Vertical resolution impacts explicit simulation of deep convection

A. M. Jenney[1]**, S. L. Ferretti**[1]**, M. S. Pritchard**[1]

[1]Department of Earth System Science, University of California, Irvine, Irvine, California

Key Points:

- The updraft mass flux and detrainment both decrease with increasing vertical resolution in SAM
- Anvil cloud fraction decreases with increasing vertical resolution in SAM
- Unrealistic boundary layer drying with convective aggregation occurs at very coarse vertical resolution

Corresponding author: Andrea Jenney, `ajenney@uci.edu`

Abstract

Vertical resolution is an often overlooked parameter in simulations of convection. We explore the sensitivity of simulated deep convection to vertical resolution in the System for Atmospheric Modeling (SAM) convection resolving model. We analyze simulations run in tropical radiative convective equilibrium with 32, 64, 128, and 256 vertical levels in a small (100 km) and large domain (1500 km). At high vertical resolution, the relative humidity and anvil cloud fraction are reduced, which is linked to a reduction in both fractional and volumetric detrainment. This increases total atmospheric radiative cooling at high resolution, which leads to enhanced surface fluxes and precipitation, despite reduced column water vapor. In large domains, convective aggregation begins by simulation day 25 for simulations with 64 and 128 levels, while onset is delayed until simulation day 75 for the simulation with 32 vertical levels. Budget analyses reveal that mechanisms involved in the generation and maintenance of convective aggregation for the 32-level simulation differ from those for the 64- and 128-level simulations. Weaker cold pools in the 32-level simulation allow the boundary layer in dry regions to become extremely dry, which leads to an aggregated state with very strong spatial gradients in column-integrated moist static energy. Understanding both the triggering and maintenance of convective aggregation and its simulated sensitivity to model formulation is a necessary component of atmospheric modeling. We show that vertical resolution has a strong impact on the mean state and convective behavior in both small and large domains.

Plain Language Summary

We study the simulation of clouds and storms in simple computer models of the tropical atmosphere. These computer models are designed so that calculations of air movement are made on a grid. This makes the atmosphere look like a very pixelated video when the grid boxes are large, and a clear high resolution video when the grid boxes are very small. Ideally, the size of these grid boxes shouldn't affect the average air movement, clouds, and rain simulated by these models. Instead, the hope of the people who use and create these computer models is that using small grid boxes just provides more detail. However, here we show that the height of grid boxes influences average properties of the simulations, such as the total cloud amount, the amount of rain that falls, and the relative humidity.

1 Introduction

Simulations of deep convection with convection resolving models (CRMs) are useful for understanding physical processes and mechanisms involved with precipitation and convective-scale atmospheric motions, including the generation and maintenance of organized tropical convection. For example, due to their ability to resolve convective-scale turbulent motions, CRMs continue to be popular tools used to inform convective parameterizations (e.g., Wang et al., 2022).

In simulations of radiative-convective equilibrium with sufficiently large limited-domain CRMs and with Earth-sized global circulation model (GCM) simulations, there is a tendency for convection to organize into one or multiple large clusters (reviewed in Wing et al., 2017). This behavior is referred to as convective aggregation. When convection transitions from spatially disorganized to an aggregated state, the tropospheric humidity distribution widens and total atmospheric radiative cooling increases (e.g., Wing & Emanuel, 2014), and simulated high cloud amount decreases while low cloud amount increases (Wing & Cronin, 2016). Tropical convection is observed to frequently organize on Earth as well (e.g., Tobin et al., 2012). Thus, better understanding mechanisms involved in simulated convective aggregation may help better understand underlying processes driving the variability of convective aggregation on Earth. Furthermore, understanding both the triggering and maintenance of convective aggregation and its simulated sensitivity to model formulation is a necessary component of making and interpreting future predictions of global climate change.

Simulated convective aggregation is sensitive to both horizontal resolution and domain size. Typically, convection only aggregates when domains are larger than 200 km, and more readily when horizontal grid spacing exceeds 2 km (Muller & Held, 2012; Yanase et al., 2020). This is because simulated convective aggregation requires net export of moist static energy from dry regions into convecting regions, which typically occurs through low-level circulations driven by strong radiative cooling from low clouds in dry columns (e.g., Bretherton et al., 2005; Coppin & Bony, 2015; Muller & Held, 2012; Muller & Bony, 2015; Yanase et al., 2020). Large domains permit stronger upgradient circulations that can fight boundary layer moisture homogenization by cold pools (Jeevanjee & Romps, 2013; Yanase et al., 2020). Coarse horizontal resolution typically results in larger amounts of simulated low clouds because of insufficiently simulated fine-scale eddies acting across sharp thermodynamic gradients atop the mixed layer (Muller & Held, 2012; Khairoutdinov et al., 2009; Pauluis & Garner, 2006; Yanase et al., 2020).

Few studies, however, have specifically investigated the sensitivity of convective aggregation to *vertical* resolution. However, given the sensitivity of simulated clouds to vertical resolution, it is reasonable to expect convective aggregation may behave differently at different vertical grid spacings. Anvil clouds are particularly sensitive to model vertical resolution (Ohno & Satoh, 2018; Ohno et al., 2019; Seiki et al., 2015; Gu et al., 2011). Because of their strong limiting effect on atmospheric radiative cooling, it is reasonable to expect that a change in anvil cloud coverage with vertical resolution may affect upgradient circulations driven by low clouds in dry columns due to impacted net radiative cooling at low cloud tops, which may then affect convective aggregation. Vertical resolution also impacts the simulation of low clouds, with finer vertical grid spacing better able to reproduce both the observed mid-tropospheric cloud top mode associated with temperature inversions near the freezing level (Inness et al., 2001; Khairoutdinov et al., 2009; Retsch et al., 2017; Roeckner et al., 2006), and boundary layer clouds, which are sensitive to the simulated structure of the layer's thermodynamics and turbulence (Bretherton et al., 1999; Guo et al., 2008; Stevens et al., 2003, 2005; Marchand & Ackerman, 2010). Thus, one way that vertical resolution may impact convective aggregation is through an impact on simulated low cloud amount.

The rate at which cloudy, humid air mixes with relatively dry, cloud-free air directly influences cloud buoyancy (Holloway & Neelin, 2009; Kuang & Bretherton, 2006; Molinari et al., 2012; Romps & Kuang, 2010; Singh & O'Gorman, 2013, 2015; Zipser, 2003), the distribution of cloud top heights (e.g., Carpenter et al., 1998; Derbyshire et al., 2004), the humidity of the cloud-free environment (Romps, 2014; Singh et al., 2019), and the thermal stratification of the tropical upper troposphere (Singh & O'Gorman, 2013, 2015). Mixing also impacts convective aggregation. Tompkins and Semie (2017) argue that strong mixing rates, which more readily dilute and suppress the vertical growth of clouds in dry regions, are necessary for convective aggregation in simulations. Becker et al. (2017) emphasize the key role of mixing by entrainment in the sensitivity of convective aggregation to sea surface temperature: at high temperatures, mixing of dry, environmental air into updrafts reduces updraft buoyancy more than at cold temperatures, thus encouraging convection to aggregate more readily.

In simulations, grid resolution is a control on mixing rates. In global CRM simulations with NICAM, Ohno et al. (2019) show a strong dependence of turbulent mixing rates on vertical resolution. They found significantly stronger turbulent diffusivity at coarse vertical resolution (38 vertical levels), leading to nearly double the global ice cloud coverage (21.5%) of identical simulations with high vertical resolution (13.5% for 398 vertical levels). This sensitivity was attributed to a dependence of the turbulent diffusivity in their simulations' sub-grid scale (SGS) mixing parameterization on local vertical grid spacing. Parishani et al. (2017) show that refining the vertical mesh of CRMs embedded in a superparameterized climate model led to increases in boundary layer vertical velocity variance. Mixing rates also depend on simulation grid spacing independent of numerical sensitivities of SGS mixing parameterizations on resolution. Jeevanjee and Zhou (2022) show a similar dependence of ice cloud coverage to *horizontal* resolution in simulations with GFDL's FV^3, where no SGS mixing scheme is employed. They find the highest ice cloud coverage in their simulations with the finest horizontal grid spacing. They hypothesize this is a result of more efficient mixing at high horizontal resolution which leads to more evaporation of condensed water in the free-troposphere. Hence, larger convective mass fluxes then produce the same amount of net latent heating needed to balance radiative cooling (which they hold constant in their simulations). Given the dependence of mixing rates on resolution, and the dependence of simulated convective aggregation on mixing rates, another way that vertical resolution may impact convective aggregation is via a control on turbulent mixing.

Vertical resolution may also impact convective aggregation via an effect on simulated cold pools, the intensity and dissipation of which are sensitive to grid resolution (Bryan & Morrison, 2012; Grant & van den Heever, 2016). Previous studies also emphasize the importance of spatially varying surface fluxes for convective aggregation (Bretherton et al., 2005; Muller & Held, 2012; Wing & Emanuel, 2014). Observational studies demonstrate that surface fluxes are also sensitive to convective aggregation (Tobin et al., 2012). To the extent that vertical resolution impacts surface fluxes, feedbacks involving surface fluxes may be involved in determining the sensitivity of convective aggregation to vertical resolution.

Vertical resolution is an often overlooked free parameter in simulations of convection, especially of convective aggregation. In this study, we explore the impact of vertical resolution on the simulated behavior of deep convection, with a focus on convective aggregation. We will show that vertical resolution directly impacts simulated profiles of clouds, temperature, and humidity, and affects the onset time of and equilibrium intensity of aggregated convection.

2 Methods

2.1 Simulations

We use the System for Atmospheric Modeling (SAM, version 6.10.9) in this study, described in Khairoutdinov and Randall (2003). Briefly, SAM is a non-hydrostatic anelastic model with doubly period boundary conditions, which conserves liquid water static energy. We use the original SAM1MOM single moment microphysics scheme (Khairoutdinov & Randall, 2003), the original SGS turbulence scheme (Khairoutdinov & Randall, 2003) which predicts subgrid turbulent kinetic energy, and the Rapid Radiative Transfer Model for GCM Applications (RRTMG; Clough et al., 2005; Mlawer et al., 1997). The model employs Newtonian damping in the top third of the model to prevent gravity wave reflection. Simulations are run in non-rotating radiative convective equilibrium with perpetual solar insolation set to 650.83 W m^{-2} at a zenith angle of 50.5, carbon dioxide concentrations at 355 ppm and a stratospheric ozone later. Convection is initiated by adding white noise to the initial surface air temperature field. We use an ocean surface with a constant sea surface temperature of 300 K.

We use four different vertical grids (Figure 1) with 32, 64, 128, and 256 vertical levels, which each linearly ramp from a grid spacing of 25 m to a maximum of 1500 m up to a model top with a rigid lid at 30 km, with variable time steps that are set to a maximum of 15 s, 6 s, 5 s, and 4 s, respectively. In the finest resolution simulation vertical levels are spaced less than 50 meters apart throughout the troposphere whereas in the

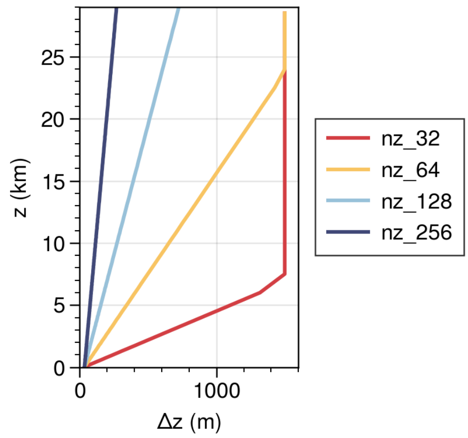

Figure 1. Grid spacing (Δz) of the vertical grids used in SAM simulations.

coarsest resolution simulation the vertical grid spacing spans many hundreds of meters, and over a kilometer in the upper troposphere.

We run two sets of simulations, one with a relatively small domain, and the other with a relatively large domain. The small domain simulations each have 128 points in the horizontal directions, with 780 m grid spacing (domain size of 99.84 km $\times$ 99.84 km). The large domain simulations each have 512 points in the horizontal directions, with 3 km grid spacing (domain size of 1536 $\times$ 1536 km). We choose these domain sizes to loosely follow the RCEMIP protocol (Wing et al., 2018), although for the large domain simulations, we use a square instead of a long channel in order to run the simulations using more parallel tasks and speed up compute time. small domain simulations are all initiated from the same warm, humid tropical sounding. large domain simulations were initialized from equilibrated small domain soundings, following Wing et al. (2018). All simulations are run for 150 days. 3D instantaneous variables (i.e., "snapshots") were saved once per day for small domain simulations and once every 12 hours for large domain simulations. 1D and 2D column integrated or surface level statistics, which represent averages across all model time steps, were saved more frequently. We do not run a large domain simulation at the highest vertical resolution (256 vertical levels) because of the high computational expense.

2.2 Diagnostics

In our analysis of convective aggregation, we use a mass weighted vertical integral of frozen moist static energy, $\langle h_f \rangle$, the spatial variance of which is a commonly used metric for convective aggregation (e.g., Wing & Emanuel, 2014; Holloway & Woolnough, 2016; Becker et al., 2017; Patrizio & Randall, 2019; Huang & Wu, 2022; Matsugishi & Satoh, 2022).

$$\langle h_f \rangle = \frac{1}{g} \int_{p_{top}}^{p_{bottom}} (c_p T + gz + L_v q_v - L_f q_i) dp, \tag{1}$$

In equation (1), g is the gravitational acceleration, p is pressure (with subscripts referencing values at model top and bottom), c_p is the specific heat capacity of dry air at constant pressure, T is air temperature, z is altitude, L_v and L_f are the latent heat of vaporization and fusion, respectively, and q_v and q_i are the mixing ratios of water vapor and condensed ice (cloud plus precipitating).

We investigate physical mechanisms that influence tendencies of the spatial variance of $\langle h_f \rangle$ as in many previous studies (e.g., Arnold & Putman, 2018; Becker et al., 2017; Beydoun & Hoose, 2019; Carstens & Wing, 2022; Chen & Wu, 2019; Coppin & Bony, 2015; Holloway & Woolnough, 2016; Huang & Wu, 2022; Matsugishi & Satoh, 2022; Patrizio & Randall, 2019; Wing & Emanuel, 2014; Wing & Cronin, 2016). The budget equation for $\langle h_f \rangle$ is

$$\frac{\partial \langle h_f \rangle}{\partial t} = LW + SW + SEF - \nabla_h \cdot \langle h_f \vec{\mathbf{u}} \rangle, \tag{2}$$

where LW and SW are the net atmospheric vertical convergences of longwave and shortwave radiation, respectively, SEF is the surface latent plus sensible heat flux into the atmosphere, and $-\nabla_h \cdot \langle h_f \vec{\mathbf{u}} \rangle$ is the column integrated horizontal flux convergence of h_f. Following Wing and Emanuel (2014), we horizontally linearize equation 2 and multiply by $\langle h \rangle'$ to obtain the budget equation for the spatial variance of $\langle h_f \rangle$:

$$\frac{1}{2}\frac{\partial \langle h_f \rangle'^2}{\partial t} = \langle h_f \rangle' \left[LW' + SW' + SEF' - \nabla_h \cdot \langle h_f \vec{\mathbf{u}} \rangle' \right], \tag{3}$$

where primes represent deviations from the horizontal domain-mean. In practice, we calculate each term except the last term on the right hand side using daily means of simulation output, and calculate the flux convergence term as a residual from this budget as was done in Bretherton et al. (2005), Muller and Held (2012), and Wing and Emanuel (2014).

Finally, we summarize the spatial organization of the large domain simulations during various periods by reorganizing the 2D horizontal space into 100-element, 1D column relative humidity percentiles, and conditioning state variables therein. We define column relative humidity as the mass weighted vertically integrated water vapor (precipitable water) divided by the precipitable water of the same column at water vapor saturation. We calculate the mass streamfunction, Ψ, in column relative humidity percentile space as in Bretherton et al. (2005) and Schulz and Stevens (2018), as

$$\Psi_i(z) = \Psi_{i-1}(z) + \overline{\rho}(z) w_i(z) \alpha \tag{4}$$

where i is an index referencing the column relative humidity percentile bin, $\overline{\rho}$ is the mean density profile, w is the vertical velocity binned by column relative humidity percentile, and α is a weight given by 1 divided by the number of bins. Ψ is calculated by starting at the driest bin and assuming $\Psi = 0$ there. This method yields closed streamfunction contours because the simulations conserve mass and have no net circulation.

3 Results

3.1 Small domain simulations

We first focus on the non-aggregated limit by analyzing small domain simulations. Here, our purpose is to assess the degree to which vertical resolution affects specific processes in the absence of large-scale convective organization, which otherwise tends to dominate statistics of radiative-convective equilibrium (e.g., Becker et al., 2017). We begin by analyzing time-mean profiles. Then, we look at how differences between the simulations evolve with time.

3.1.1 Time-mean profiles

Unless otherwise noted, all presented results in this section are for the average across days 50 to 150. We use the naming convention "nz_X" where X represents the number of vertical levels in each model run. That is, "nz_32" uses the coarsest vertical resolution of over 1 km grid spacing in the upper troposphere, whereas "nz_256" uses the finest.

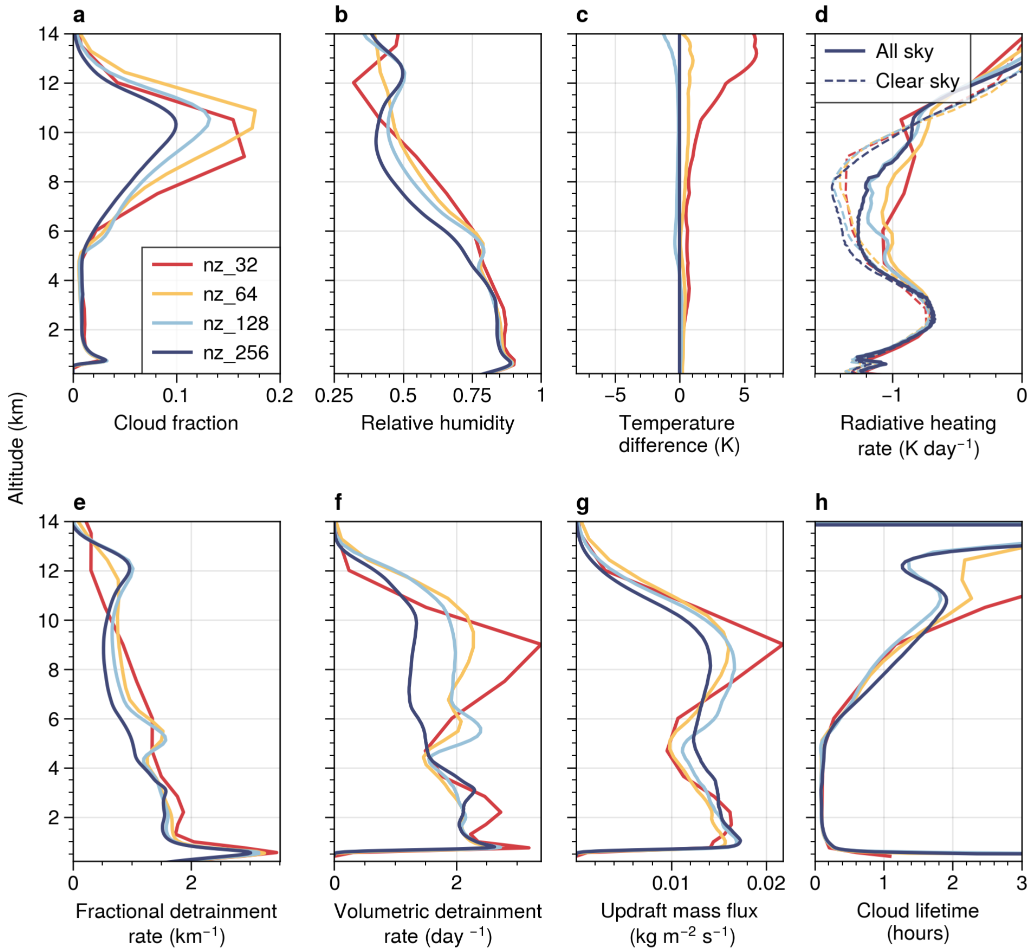

Figure 2. Horizontal averages from simulation days 50-150 for small domain simulations of (a) cloud fraction, (b) relative humidity, (c) temperature difference from nz_256, (d) all-sky and clear-sky radiative heating rates, (e) fractional detrainment rate, δ, (f) volumetric detrainment rate, $\delta M_u/\rho$, (g) updraft mass flux, and (h) cloud lifetime.

Figure 2 shows time and horizontally averaged profiles for the simulations. Consistent with Ohno et al. (2019), high cloud fraction is sensitive to vertical resolution, especially above 7 km, with the coarsest resolution simulations producing the highest cloud fraction, and with cloud fraction generally decreasing with increasing vertical resolution. Here, we define cloud fraction at each time and each model level as the fraction of grid cells with cloud condensate mixing ratios above 5 $\times 10^{-3}$ g kg^{-1}. Consistent with previous studies, the relative humidity is sensitive to vertical resolution (Figure 2b), with the most humid mean profile in the lowest resolution case, and the driest mean profile in the highest resolution case (Tompkins & Emanuel, 2000; Roeckner et al., 2006). Later, we will show that this is related to differences in fractional detrainment. Figure 2c shows the mean temperature profile deviation from that of nz_256. The mean temperature is roughly the same between the nz_128, and nz_256 cases, with the nz_32 and nz_64 cases warmer than the others, especially above 10 km. This is consistent with other studies (Lee et al., 2019; Roeckner et al., 2006; Tompkins & Emanuel, 2000), who find colder upper tropospheres when using higher vertical resolution. Between roughly 5-10 km, the radiation profiles diverge from each other (Figure 2d), with the magnitude of radiative cooling increasing with grid resolution. Consistent with the spread in relative humidity, there is spread in the clear-sky radiative cooling rate, with mid-tropospheric radiative cooling increasing with increasing vertical resolution: a drier, more emissive state. Between 4-10 km, there is additional spread in the all-sky radiative cooling rate, likely driven by differences in longwave backradiation due to anvil cloud coverage, e.g. fewer high clouds at nz_256 permitting enhanced all-sky cooling from the mid-troposphere. We now implicate varying rates of detrainment in the sensitivity of relative humidity to vertical resolution (Figure 2b). Romps (2014) and Singh et al. (2019) derive a diagnostic, steady-state equation for the relative humidity, RH, as a function of the fractional detrainment rate, δ:

$$RH = \frac{\delta}{\delta + \gamma}, \tag{5}$$

where $\gamma = -\partial_z \ln(q_v^*)$, with q_v^* the saturation specific humidity and z the altitude. Equation (5) describes relative humidity as the balance between moistening through convective detrainment (with a length scale given by δ), and drying via subsidence (with a length scale given by γ). We can rewrite (5) to obtain a diagnostic, steady-state relation for the fractional detrainment rate as a function of the relative humidity. Estimates of δ from steady-state temperature and relative humidity are shown in Figure 2e. Throughout most of the troposphere, δ generally decreases as grid resolution increases. We find that differences in δ, rather than in temperature, explain differences in relative humidity between the simulations (Figure S1).

Next, we explore the sensitivity of high cloud coverage to vertical resolution. Time-mean anvil cloud fraction is, to first order, a product of the volumetric detrainment rate and cloud lifetime (Beydoun et al., 2021; Jeevanjee & Zhou, 2022; Seeley et al., 2019). We diagnose the volumetric detrainment rate as $\delta M_u/\rho$, where M_u is the steady-state updraft mass flux and ρ is the air density. We define $M_u = \rho w_u \sigma_u$, where w_u is the mean updraft vertical velocity and σ_u is the fractional updraft area, and "updrafts" are grid cells with ascending vertical velocities exceeding 0.5 m s^{-1} and cloud condensate mixing ratios exceeding 0.1 g kg^{-1} (although results are not sensitive to these thresholds). Profiles of the volumetric detrainment rate are shown in Figure 2f. We point out that the profiles of volumetric detrainment computed this way have the same magnitude and shape as volumetric detrainment profiles computed using steady-state cloud water source and sink rates (Jeevanjee & Zhou, 2022). Above 6 km, there is a large decrease in volumetric detrainment with increasing vertical resolution. The shapes of the volumetric detrainment rate and anvil cloud fraction are quite similar, thus it seems that spread in $\delta M_u/\rho$ is driving the spread in anvil cloud fraction. We include profiles of the updraft mass flux (Figure 2g) for reference.

Finally, we compute anvil cloud lifetimes as a residual by dividing the anvil cloud cloud fraction by the volumetric detrainment rate, $\delta M_u/\rho$. This is shown in Figure 2h. Cloud lifetimes are roughly equal below 10 km. Between 10-13 km, anvil cloud lifetime is small at high vertical resolutions and large at low vertical resolutions. We think this may be related to a sensitivity of the ice sedimentation parameterization to vertical resolution in SAM1MOM, although we do not investigate this further. Nonetheless, we confirm that sensitivity of the volumetric detrainment rate to vertical resolution, driven primarily by spread in the updraft mass flux, but also by the fractional detrainment rate, is driving spread in the anvil cloud fraction.

One way we expect vertical resolution to explicitly affect CRM simulations is via a control on mixing. Updrafts may detrain mass to the environment either by mixing partially with the environment such that there is an exchange (mixing) of air between humid updraft air and the dry environmental air during ascent, or when updraft velocity reaches zero, typically at an ascending parcel's level of neutral buoyancy. Given the limited data output, we are unable to directly calculate the so-called turbulent versus organized detrainment rates for these simulations. However, the shape of the fractional detrainment rate profiles in Figure 2e suggest stronger mixing rates at coarse vertical resolution.

Jeevanjee and Zhou (2022) showed that horizontal resolution affects mixing rates. In simulations of radiative-convective equilibrium, the heating rate associated with the updraft mass flux must balance the net atmospheric radiative cooling rate. Because mixing causes evaporation of condensed water, which cools the atmosphere, Jeevanjee and Zhou (2022) argue that simulations with stronger mixing produce larger updraft mass fluxes in order to compensate for the enhanced mixing-driven evaporative cooling. Higher anvil cloud fractions occur as a result of larger mass fluxes. Here, larger updraft mass fluxes, upper-level detrainment rates, and anvil cloud fractions for the coarse resolution simulations are all consistent with our assessment that the coarse vertical resolution simulations are mixing more.

In most of the vertical profiles in Figure 2, the nz_64 and nz_128 simulations contain a "kink" at or near 5 km (near the freezing level), which is due to enhanced simulation of the congestus cloud mode (Johnson et al., 1996) for these resolutions. Figures 2e,f show that there is a local maximum of detrainment at these levels. The coincident sharp increase in the updraft mass flux for these two simulations suggests large entrainment rates. This enhanced mixing of moist updraft air with environmental air at this level drives an increase in relative humidity (2c) (Sokol & Hartmann, 2022). A similar feature is also apparent in the static stability profile, with a layer of enhanced stability located atop of a layer of reduced stability (not shown). These features, which are not present in the initial sounding, are related to the emergence of a congestus cloud mode, visible on the cloud fraction profiles of the nz_64 and nz_128 simulations.

Enhanced mid-level cloud detrainment has been argued to be due to the presence of a mid-tropospheric stable layer. This layer has been argued to be due to latent heat release from ice melting (Johnson et al., 1996; Mapes & Houze, 1995). It has also been argued to result from differential radiative destabilization of the lower and upper troposphere due to vertically-varying water vapor which creates a mid-level mode in the distribution of levels of neutral buoyancy (Nuijens & Emanuel, 2018). Sokol and Hartmann (2022) argue that congestus detrainment in CRMs is driven by compensating horizontal convergence into regions of radiatively driven vertical mass divergence. Regardless of the reason for initial congestus level detrainment, a mid-tropospheric stable layer persists due to a feedback involving strong radiative cooling at cloud tops under a dry upper troposphere, which fuels further local detrainment either through the intensification of the stable layer (which reduces updraft buoyancy) or by driving mid-level vertical mass divergence (which must be balanced in radiative-convective equilibrium by mid-level con-

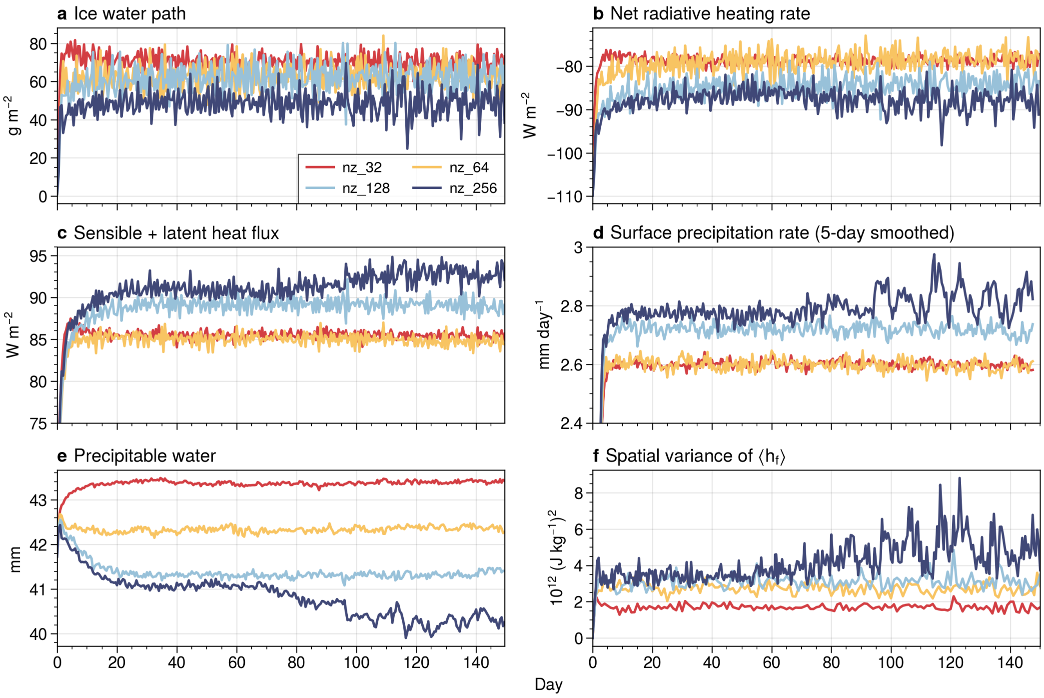

Figure 3. For small domain simulations, 12-h means of (a) ice water path, (b) net radiative heating rate of the atmosphere (net top-of-atmosphere flux minus net surface flux), (c) sensible plus latent heat flux, (d) surface precipitation rate, (e) precipitable water, and (f) spatial variance of vertically integrated frozen moist static energy. A centered running-mean window of 5 days has been applied to the 12-h precipitation rate.

vective detrainment) (Mapes & Zuidema, 1996; Posselt et al., 2008; Sokol & Hartmann, 2022).

Previous studies find an increase in the simulation of the congestus cloud mode with vertical resolution in both simulations with parameterized (Inness et al., 2001; Retsch et al., 2017; Roeckner et al., 2006) and explicit convection (Khairoutdinov et al., 2009). Puzzlingly, we find that the congestus mode detrainment and associated structures in relative humidity, dry static stability, and cloud fraction are absent in both our highest and lowest vertical resolution cases.

3.1.2 Time-evolution

We now explore the time evolution of differences in the small domain simulations. Spread in ice cloud coverage, which we showed in the previous section is primarily driven by differences in the updraft mass flux and volumetric detrainment rates, is established quickly by day 2, with equilibrium amounts established after about 10 days (Figure 3a). The net atmospheric radiative heating rate (calculated as the difference between the net radiative flux at the surface and the net radiative flux at the top of the atmosphere) is immediately affected (Figure 3b), with the highest resolution simulations cooling more due to their lower ice cloud coverage and lower free-tropospheric relative humidities (the combination of which leads to high transmissivity of radiation emitted from low levels). Surface fluxes and precipitation similarly adjust, with higher values for nz_128 and nz_256 needed to balance the additional atmospheric longwave cooling (Figure 3c,d). Figure 3e shows the time evolution of domain mean precipitable water. Figure 2c,d show that the model spread is due to a combination of both the coarse resolution simulations having higher mean relative humidities and temperature. The change in column water vapor with resolution is opposite to that of precipitation, implying that precipitation is more efficient at high vertical resolution. This highlights how vertical resolution may cause deviations to the mean precipitation rate from that expected due to moisture.

While equilibrium precipitation rates and precipitable water are established by day 20 for all simulations, shortly before day 80, nz_256 begins to dry further, and develops increased variance in moisture and precipitation, suggesting that it is starting to aggregate (Held et al., 1993). Time series of the spatial variance of frozen moist static energy ($\langle h_f \rangle'^2$, see section 2.2) (Figure 3e) show increases for nz_256 at the same time that precipitable water decreases, indicating that dry regions are growing as convection becomes more organized. Visual inspection of snapshots of precipitable water at the end of the simulation confirm that dry regions are drying further and growing in horizontal extent (Figure S3), although convection is not quite yet aggregated into one connected region.

These signs of developing convective aggregation are surprising given the small domain (about 100 km) and relatively high horizontal resolution (780 m). Typically, at horizontal resolutions less than 2 km, domain sizes of about 500 km are needed for the aggregation of convection (Muller & Held, 2012; Yanase et al., 2020). This is because cold pool circulations spread moisture into dry regions surrounding convection, which can homogenize boundary layer moisture when the domain is small (Jeevanjee & Romps, 2013; Yanase et al., 2020). This suggests that in nz_256, there is one or multiple physical mechanisms increasing moist static energy in humid columns, and/or removing moist static energy from dry columns that is strong enough to combat downgradient moistening from cold pools. This may be related or due to the very strong mid-tropospheric radiative cooling (Figure 2e) in the nz_256 simulation enabled by its high resolution.

3.2 Large domain simulations

Here, we assess the impact of vertical resolution on convective aggregation in large domain simulations. These simulations (see Section 2.1) were run with 32, 64, and 128 vertical levels for 150 days.

Unlike the small domain simulations, convection in the large domain simulations aggregates. Figure 4 shows snapshots of precipitable water from simulation days 5 and 150. On simulation day 5, all cases are disaggregated, and precipitable water is relatively homogeneous around a mean value of about 38 mm. Aggregation develops as dry subsiding patches of air gradually expand and deep convection becomes confined to a singular region. By day 150, the large dry regions that emerge in all cases are much drier than anywhere seen in the disaggregated states at day 5, and the dry regions in nz_32 are much drier than those in nz_64 or nz_128. These dry subsiding regions are associated with large-scale overturning circulations, whose fractional area grows as convection becomes more aggregated. The mid-tropospheric subsidence fraction is consequently one metric commonly used to quantify and mark the onset of convective aggregation (e.g., Coppin & Bony, 2015; Wing et al., 2020). We plot time series of the fractional area with subsiding 500 hPa daily mean vertical velocities for each simulation in Figure 5a. Around day 50, subsidence fraction increases from about 0.53 to roughly 0.57 for nz_64 and nz_128, suggesting this is near when aggregation occurs. Additionally, the temporal variance of the subsidence fraction for these two simulations increases at this time as well. Meanwhile, nz_32 remains at the same subsidence fraction throughout the simulation period, with variance appearing to begin to grow by day 140.

Time series of $\langle h_f \rangle'^2$ more clearly show the onset of convective aggregation in the large domain simulations (Figure 5b). This occurs around the same time for nz_64 and nz_128, with an onset period between roughly day 20 and day 60, with nz_128 appearing to aggregate between 5-10 days before nz_64. Beyond day 60, convection remains ag-

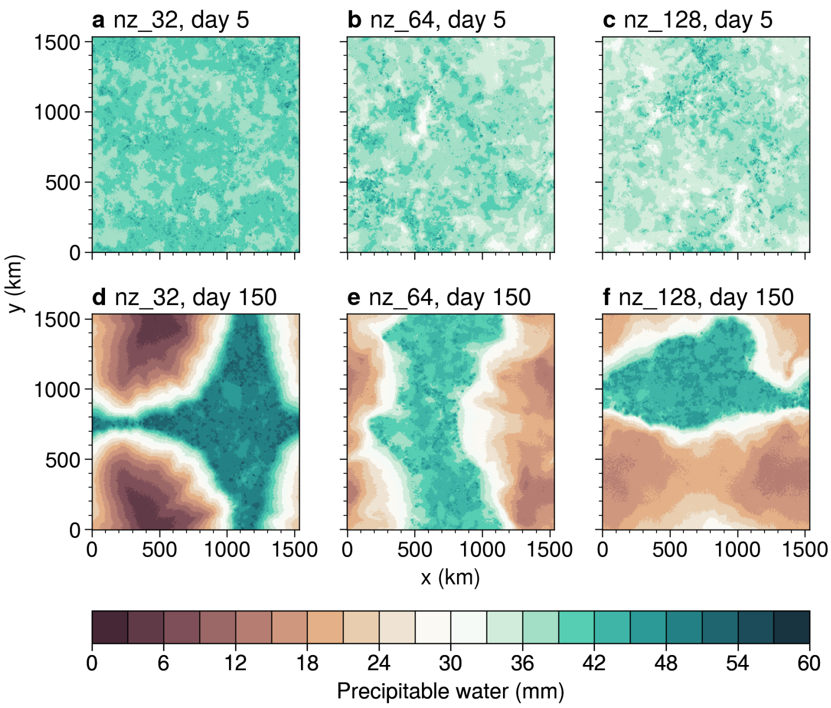

Figure 4. Snapshots of precipitable water from simulation days 5 (a-c) and 150 (d-f) for large domain simulations.

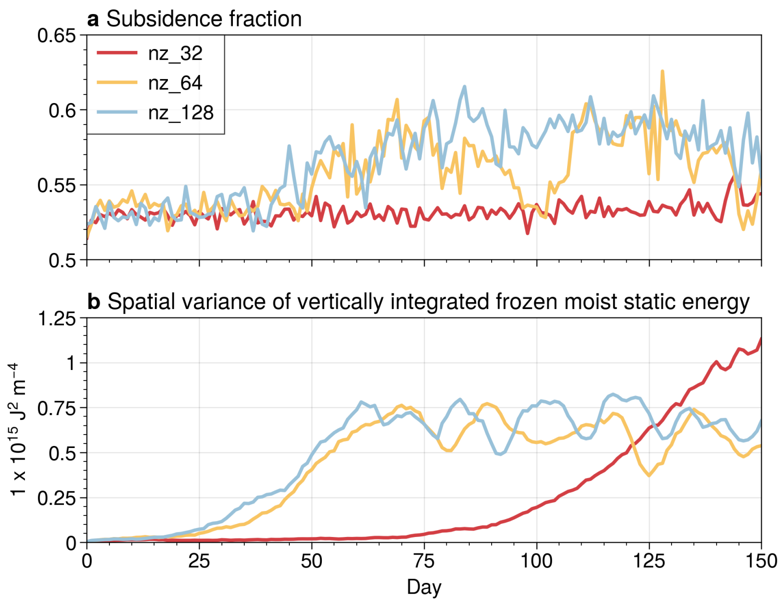

Figure 5. Daily and domain averaged (a) subsidence fraction around 500 hPa and (b) spatial variance of vertically integrated frozen moist static energy for large domain simulations.

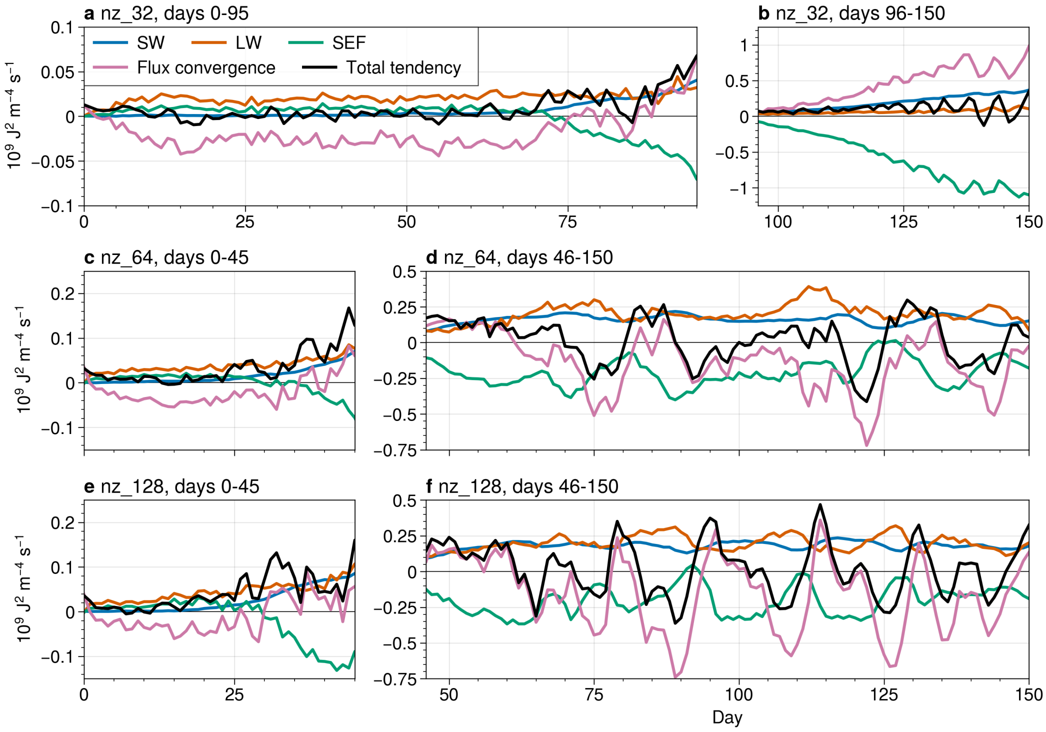

Figure 6. For large domain simulations, time series of each term in the budget equation for the tendency of $\langle h_f \rangle'^2$ (equation 3). Note the different vertical limits on each panel.

gregated for these two simulations and exhibits oscillating behavior around some equilibrium point, as in Patrizio and Randall (2019). The behavior of nz_32 is quite different. Aggregation occurs later, with an onset period that starts around day 65. The onset period of aggregation for nz_32 is long compared to nz_64 and nz_128. By day 150, it has not yet obviously reached equilibrium, and has a value of $\langle h_f \rangle'^2$ that is nearing twice as large as the equilibrium values of the other simulations. This is in part due to dry regions that contain near-zero amounts of water vapor (Figure 4d). While nz_32 has not yet reached an aggregated equilibrium value of $\langle h_f \rangle'^2$, it is beginning to show some oscillating behavior, which for the other simulations does not occur during aggregation onset but occurs at equilibrium, suggesting that nz_32 may be near equilibrium by day 150.

Next we use the $\langle h_f \rangle'^2$ budget equation (3) to investigate physical mechanisms responsible for simulated differences in aggregation between the different vertical resolutions. Figure 6 shows time series of the spatial mean of each term in equation (3) for each of the large domain simulations. We have split the time dimension into two periods to better differentiate terms during the early onset period (left panels), which are relatively small in amplitude. We begin by looking at the first 25 days of each simulation. During this time, the tendency of $\langle h_f \rangle'^2$ is small, with positive contributions from the longwave and surface flux terms balanced by negative contributions from the $\langle h_f \rangle$ flux convergence terms.

Next we visualize how clouds, radiation, and the overturning circulation are organized in moisture space during the early period of each simulation. Figure 7 shows the radiative cooling rate, mass streamfunction (Ψ, see equation 4 in section 2.2), cloud condensate mixing ratio, and h_f binned by column relative humidity percentile for days 0-25. The spatial organization of these fields is relatively similar between the simulations.

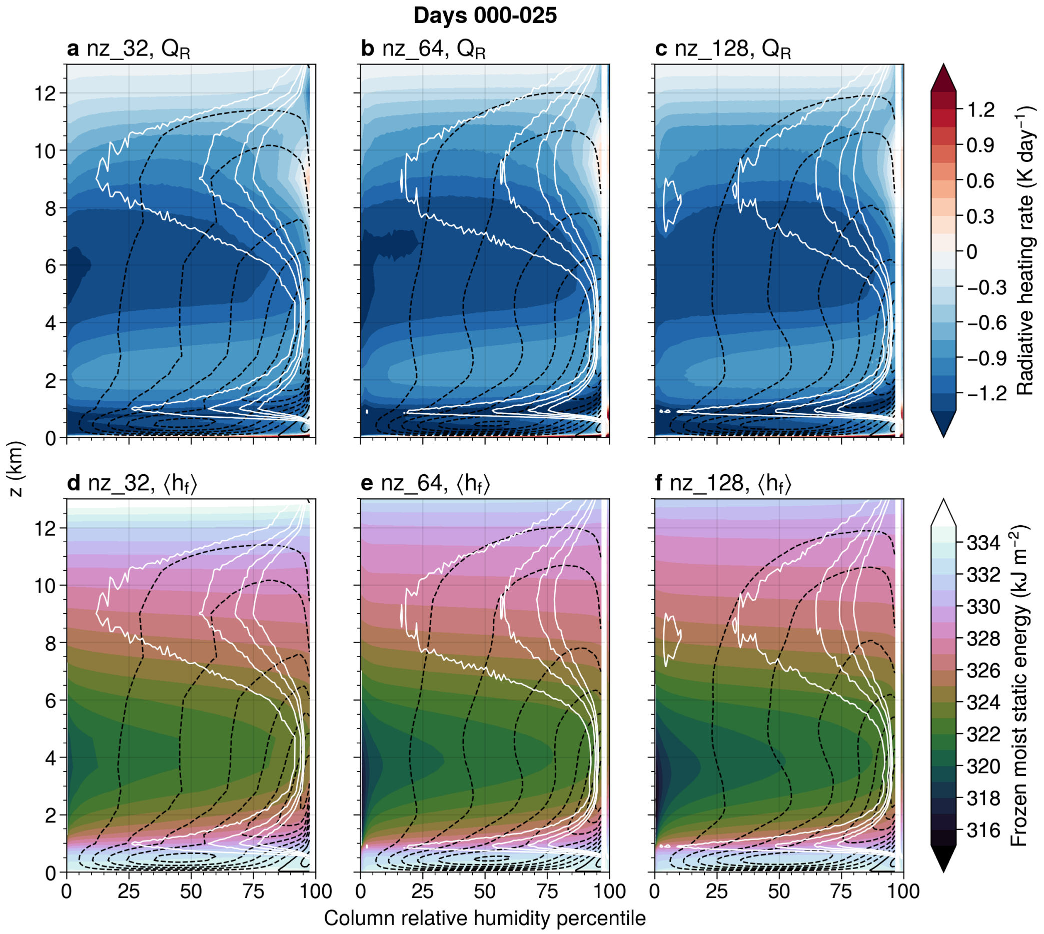

Figure 7. For large domain simulation days 0-25, (a-c) radiative heating rate (filled contours), cloud condensate mixing ratio (white contours drawn at 3×10^{-3} g kg^{-1}, 6×10^{-3} g kg^{-1}, 9×10^{-3} g kg^{-1}, and 12×10^{-3} g kg^{-1}), and mass streamfunction (black contours drawn every 1 g m^{-2} s^{-1}), each binned by column relative humidity percentile. (d-f) As in top row but filled contours show h_f.

However, we note that as in the small domain simulations, there is larger anvil cloud coverage at low vertical resolution (white contours between 8-11 km in Figure 7a,b,c extend further into dry columns at coarse resolution than at high resolution). The reverse is true for low clouds, with cloud coverage at 1 km extending further into the dry region at high resolution. Generally, Ψ has a similar shape and magnitude in each of the simulations, although there appears to be additional mid-level horizontal motion in nz_64 and nz_128, consistent with enhanced congestus divergence in the small domain simulations at these resolutions. Finally, the mid-tropospheric h_f minimum over dry columns is strongest in the high resolution simulation, despite relatively weaker mid-level radiative cooling in those columns.

Aggregation onset for nz_64 and nz_128 occurs around days 25 and 17, respectively, when the total tendency of $\langle h_f \rangle'^2$ begins increasing. In order to look more closely at the budget terms shortly before these days, Figure 8 shows instantaneous (left column) and cumulative (right column) tendencies zoomed in for days 0-25 of all simulations. Figure 8j, the cumulative total tendency of $\langle h_f \rangle'^2$ (integrated from day 0), shows increases in the slope of the total tendency for nz_64 and nz_128 around days 25 and 17, respectively, confirming that these days mark the onset of accelerated aggregation. Consistent with previous studies, this initiation of convective aggregation for both vertical resolutions appears to be largely due to horizontal covariances in longwave and surface flux anomalies with $\langle h_f \rangle$ anomalies (e.g., Bretherton et al., 2005; Muller & Held, 2012), which are both positive from the start of the simulations until aggregation begins. Shortly before aggregation, the shortwave term begins growing as well, although its contribution to the total tendency is an order of magnitude smaller. The $\langle h_f \rangle$ flux convergence term is negative during this early period.

While both nz_64 and nz_128 have begun aggregating by day 25, nz_32 has not (Figure 5b, 6a). The cumulative tendency of $\langle h_f \rangle'^2$ and its budget terms (right column of Figure 8) offers some insight into this difference. For the first 25 days for all simulations, the cumulative tendency of $\langle h_f \rangle'^2$ due to shortwave, longwave, and surface fluxes is positive and increasing. Similarly, the cumulative tendency of $\langle h_f \rangle'^2$ due to the horizontal flux convergence of $\langle h_f \rangle$ is negative and also increasing in magnitude for all simulations. This illustrates a competition between homogenization of $\langle h_f \rangle$ by horizontal circulations (the flux convergence term), and the increase in $\langle h_f \rangle'^2$ by diabatic processes for all simulations over the first 25 days. Aggregation occurs in nz_64 and nz_128 because, taken together, the diabatic processes that increase $\langle h_f \rangle'^2$ are increasing $\langle h_f \rangle'^2$ faster than horizontal circulations can homogenize it. However, in nz_32, the cumulative tendency of $\langle h_f \rangle'^2$ remains steady after about day 8 because there is a balance between the diabatic terms and the adiabatic term. Additionally, each budget term for nz_32 is smaller than those for nz_64 and nz_128. Therefore, aggregation is not occurring in nz_32 because diabatically driven increases in $\langle h_f \rangle'^2$ by radiative processes and surface fluxes are too weak to overcome horizontal $\langle h_f \rangle$ homogenization by horizontal circulations.

We now look at simulation days 25-50, during which nz_64 and nz_128 are becoming more aggregated (that is, $\langle h_f \rangle'^2$ is increasing) (Figure 5b), and nz_32 remains disaggregated. The continued increase in $\langle h_f \rangle'^2$ for both nz_64 and nz_128 is now driven by increases in the horizontal covariances of radiative anomalies and $\langle h_f \rangle$ flux convergence anomalies with $\langle h_f \rangle$ anomalies (Figure 6c,e), while surface fluxes horizontally homogenize $\langle h_f \rangle$. Figure 9 shows various quantities binned by column relative humidity percentile between days 25-50. In nz_128, low cloud extent has retreated somewhat compared to days 0-25 (Figure 7). However, low cloud thickness has increased. The lower-to-mid-tropospheric (1-6 km) minimum in h_f has intensified (again, relative to days 0-25) over dry percentiles in nz_64 and nz_128, with deeper intensification in nz_128. In the boundary layer, a new horizontal gradient of h_f emerges in nz_64 and nz_128 in the driest 20% of columns, indicating that boundary layer drying through horizontal moisture export from these columns is exceeding low-level moistening through surface latent

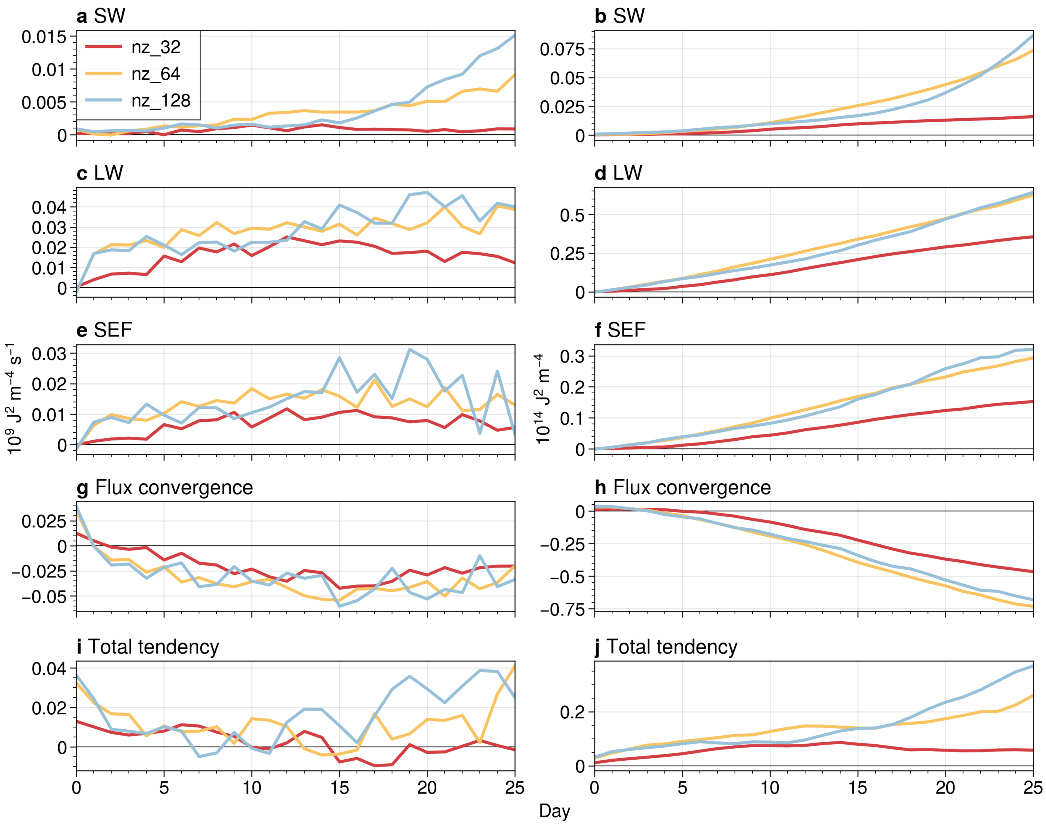

Figure 8. For large domain simulations, contributions to the total tendency of $\langle h_f \rangle'^2$ from (a) shortwave radiation, (c) longwave radiation, (e) surface fluxes, (g) horizontal $\langle h_f \rangle$ flux convergence, and (i) the total tendency. Right column shows the tendency of the same budget terms from the left column but integrated in time from simulation day 0.

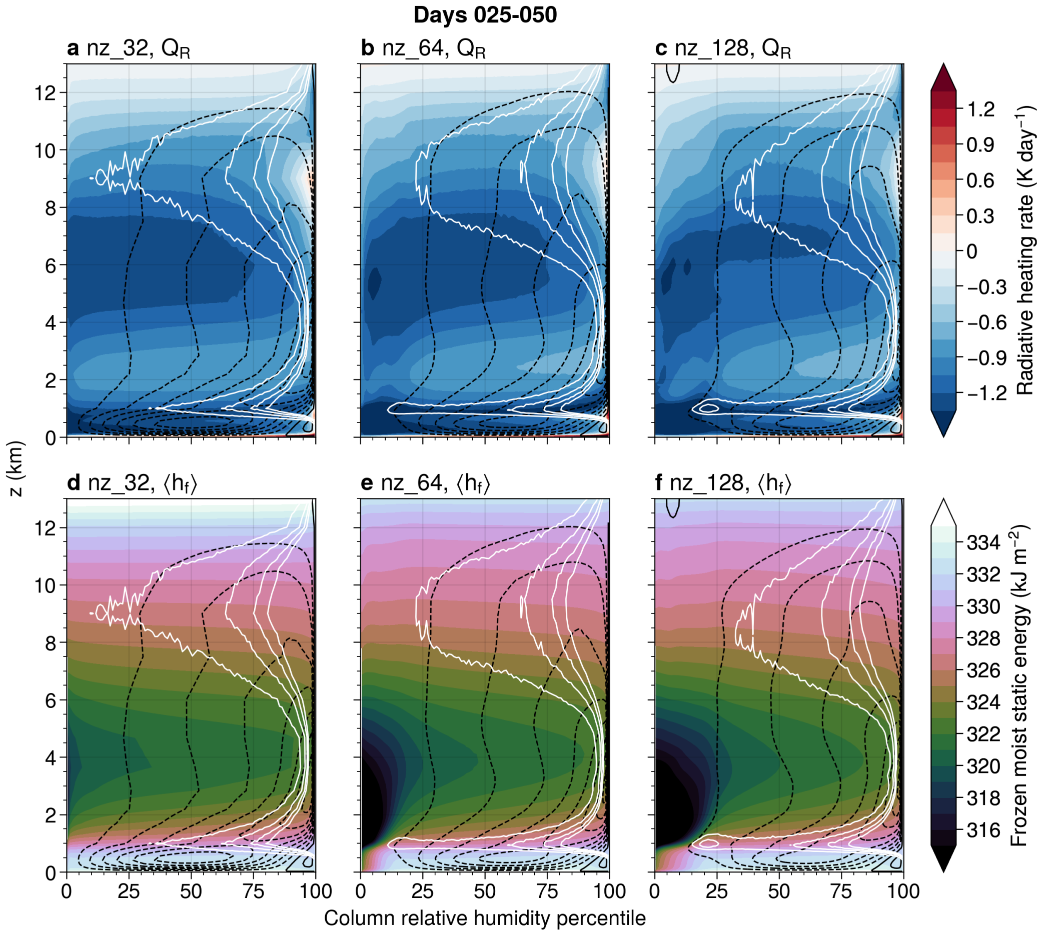

Figure 9. For large domain simulation days 25-50, (a-c) radiative heating rate (filled contours), cloud condensate mixing ratio (white contours drawn at 3×10^{-3} g kg^{-1}, 6×10^{-3} g kg^{-1}, 9×10^{-3} g kg^{-1}, and 12×10^{-3} g kg^{-1}), and mass streamfunction (black contours drawn every 1 g m^{-2} s^{-1}), each binned by column relative humidity percentile. (d-f) As in top row but filled contours show h_f.

heat fluxes. There does not appear to be much change in the structure of Ψ in any of the simulations.

Around days 60 and 70, respectively, the nz_128 and nz_64 simulations reach their simulated maximum $\langle h_f \rangle'^2$ values (Figure 5b), and begin to show oscillations in their $\langle h_f \rangle'^2$. The budget of $\langle h_f \rangle'^2$ offers some insight into the mechanisms involved in the oscillation (Figure 6), which we comment on briefly. The oscillation in $\langle h_f \rangle'^2$ closely follows the h_f flux convergence term. Rapid increases in the h_f flux convergence term appear to be preceded by increases in the surface flux term, the latter of which almost always remains a negative contribution to the total tendency, but oscillates in magnitude. In nz_128, the longwave terms appears to oscillate in phase with the surface flux term. In contrast, the shortwave term does not appear to contribute to the oscillation of $\langle h_f \rangle'^2$. While there are additional interesting features in the oscillations of $\langle h_f \rangle'^2$ and its budget terms, such as their periodicity, we do not investigate this further.

While our coarsest vertical resolution configuration did not aggregate into an oscillating equilibrium within the time scale of these simulations, it experiences a delayed

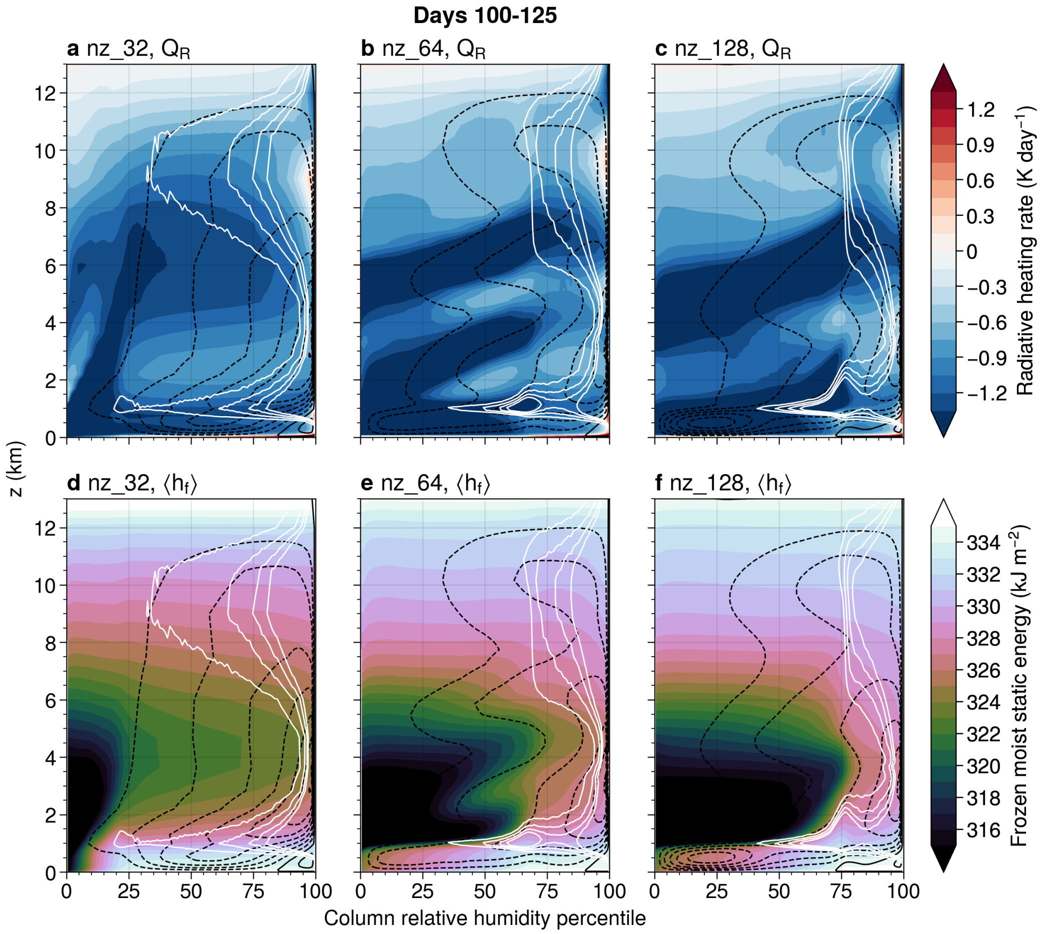

Figure 10. For large domain simulation days 100-125, (a-c) radiative heating rate (filled contours), cloud condensate mixing ratio (white contours drawn at 3×10^{-3} g kg^{-1}, 6×10^{-3} g kg^{-1}, 9×10^{-3} g kg^{-1}, and 12×10^{-3} g kg^{-1}), and mass streamfunction (black contours drawn every 1 g m^{-2} s^{-1}), each binned by column relative humidity percentile. (d-f) As in top row but filled contours show h_f.

onset and slower growth period. Around day 70, the total tendency of $\langle h_f \rangle'^2$ of nz_32 begins to grow (Figure 6a). This is due to a positive fluctuation of the $\langle h_f \rangle$ flux convergence term superimposed on a very slowly growing shortwave term (which began very slowly growing around day 45). At that point, it appears as though some critical threshold of $\langle h_f \rangle'^2$ is reached, and the same reversal of the $\langle h_f \rangle$ flux convergence and surface flux terms found in the other simulation also occurs here. Increases in the radiative and $\langle h_f \rangle$ flux convergence terms contribute to an increasing total tendency of $\langle h_f \rangle'^2$ beyond day 85. Unlike nz_64 and nz_128, where the magnitude of all terms in the $\langle h_f \rangle'^2$ budget during aggregation onset is roughly equal, for nz_32, the flux convergence term dominates the positive tendency of $\langle h_f \rangle'^2$, with the shortwave term also contributing positively at about half of the magnitude of the convergence term. In nz_32, the longwave term is roughly one tenth of the size of the convergence term. Differences in nz_32's $\langle h_f \rangle'^2$ budget from nz_64 and nz_128 will be discussed in more detail in what follows.

Figure 10 shows column relative humidity binned quantities for days 100-125, which marks the intermediate growth period of aggregation for nz_32, and mature stages of aggregation for nz_64 and nz_128. There are some notable differences for nz_32 at this point from earlier periods in the simulation: specifically, in the structure of radiative cooling in the dry regions, and in the boundary layer h_f. In columns around the 25th percentile of column relative humidity, the mid-tropospheric maximum in radiative cooling between 4-8 km has intensified from days 25-50 (Figure 9a) to days 100-125. This mid-tropospheric radiative cooling maximum now extends down to the surface, whereas before it was confined between 4-8 km. This is likely related to the structure of h_f, which shows very low values that extend down to the surface, whereas they remain relatively high below 1 km for previous times and in the other simulations. In fact, the ability of the nz_32 simulation to reduce boundary layer h_f to this degree explains why its $\langle h_f \rangle'^2$ is able to increase beyond those in the nz_64 and nz_128 simulations (Figure 5b). That is, boundary layer h_f is heavily weighted in column $\langle h_f \rangle$. Very low boundary layer h_f in dry columns in nz_32 may be related to the relative weakness of cold pools in this simulation (Figure 11), which keeps boundary layer moisture in the other simulations relatively homogeneous (Jeevanjee & Romps, 2013; Yanase et al., 2020). This is not inconsistent with having seen the reverse (more homogeneous boundary layer h_f for nz_32) during days 25-50, because nz_32 had not yet aggregated. Furthermore, the extreme relative minimum in boundary layer h_f in nz_32's dry columns also explains why the $\langle h_f \rangle$ flux divergence and surface flux terms get so large in magnitude (Figure 6b) beyond day 105. Low-level mass divergence out of the dry region efficiently exports moist static energy to more humid columns because of the intense gradient in boundary layer moist static energy. In contrast, surface fluxes in the dry region very efficiently moisten those columns (a negative feedback with $\langle h_f \rangle'^2$) because of the extreme dry boundary layer.

By days 100-125, the nz_64 and nz_128 simulations display large changes in their spatial structures of radiation, clouds, and Ψ. Consistent with Sokol and Hartmann (2022), there is an intensification of the mid-tropospheric congestus circulation with aggregation for these simulations, which is largely missing for the nz_32 simulation. This absence may be due to the fact that nz_32 is still aggregating at this time. However, the results of section 3.1, which show enhanced congestus detrainment for nz_64 and nz_128 and weak congestus detrainment for nz_32 in small domains, suggest that the coarse vertical resolution is more fundamentally to blame. Above 1 km, maxima in radiative cooling of nz_64 and nz_128 follow horizontal motion indicated by the streamfunction contours. This is consistent with the horizontal motion being associated with detrainment of clouds and moisture, with strong radiative cooling occurring at the tops of clouds and moist layers. Interestingly, there are two mid-tropospheric horizontal outflow and radiative cooling layers in nz_64 (at roughly 6 km and 2 km), with only one in nz_128 (at roughly 5 km), a feature which is robust to averaging period. This may be related to differences in the low cloud field, which has evolved substantially since days 25-50. The horizontal extent of low clouds has decreased, pulling towards more humid columns, especially in the higher

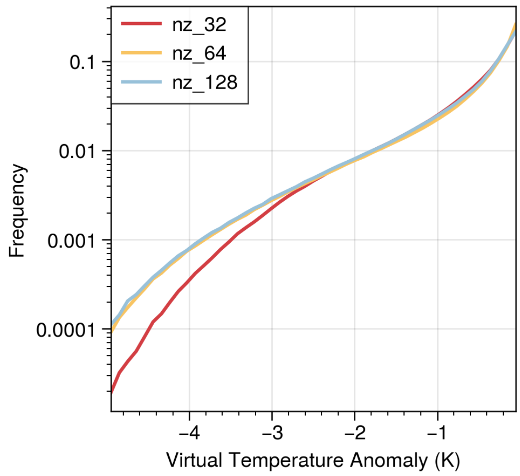

Figure 11. Distribution of instantaneous virtual temperature anomalies from the horizontal mean at the lowest model level for simulation days 0 to 30 of the large domain simulations.

resolution configurations with most mature aggregation. At the same time, the vertical extent and thickness of low clouds for columns between the 50-75th percentiles have grown, with both thickness and vertical extent enhanced in the nz_128 simulation. Finally, anvil cloud coverage in nz_64 and nz_128 are reduced, which is consistent with the decrease in the area coverage and spatial concentration of humid ascending air that accompanies aggregation (Figure 4,5a).

4 Discussion and Conclusions

We investigate the impact of varying vertical resolution on small (about 100 km × 100 km) and large (about 1500 km × 1500 km) domain simulations of explicit convection in radiative convective equilibrium. We use simulations with 32, 64, 128, and 256 vertical levels (although we do not run a large domain simulation with 256 levels because of the high computational expense).

Results of the small domain simulations show that high vertical resolution produces cooler upper tropospheres and reduced relative humidity. Differences in humidity are explained by differences in fractional detrainment. Anvil cloud coverage is markedly different between the simulations, with coarse resolution simulations producing the highest amounts. This is due to differences in volumetric detrainment, spread in which is driven primarily by spread in the updraft mass flux, but also by spread in the fractional detrainment rate. The combination of a drier free troposphere and reduced anvil cloud coverage at high vertical resolution leads to enhanced atmospheric radiative cooling, surface fluxes, and precipitation. Increases in precipitation with vertical resolution occur despite simultaneous decreases in precipitable water.

We suspect that a dependence of the turbulent mixing rate on vertical resolution is driving the simulated differences in relative humidity and anvil cloud fraction. Due to output limitations, we do not explicitly estimate turbulent mixing rates. However, because the fractional detrainment rate, δ, is in part a measure of the the rate at which updrafts lose mass through turbulent exchange with environmental air, it is plausible that decreases in turbulent mixing at least partly explain decreases in δ with increasing vertical resolution. Additionally, we find a reduced mean updraft mass flux with increased vertical resolution, which may occur because reduced mixing increases the efficiency of total heating associated with the updraft mass flux (because of reduced condensate evaporation), as was found in Jeevanjee and Zhou (2022), but in their case with horizontal resolution. Similarly, enhanced mixing at low vertical resolution, and the resultant relatively large updraft mass flux, explains both its enhanced relative humidity and anvil cloud fraction. While our lack of an explicit quantification of turbulent mixing rates and their sensitivity to vertical resolution in SAM is a weakness of our study, we note that other studies have linked low vertical resolution to stronger mixing (e.g., Bretherton et al., 1999; Guo et al., 2008; Ohno et al., 2019).

We note some interesting results for our highest resolution case (nz_256) that were counter to our expectations. It began to aggregate, which is surprising given the high horizontal resolution (780 m) and small domain size. Additionally, while we found expected enhancement in the simulated mid-level congestus mode for the two intermediate resolution cases (nz_64 and nz_128) compared to the lowest resolution case, the congestus mode was diminished for the highest resolution case (nz_256).

Unlike the small domain simulations, convection aggregated in each of the large domain simulations. Generally, nz_64 and nz_128 behaved similarly, displaying roughly similar aggregation onset times, mechanisms, and equilibrium behavior and spatial organization. In contrast, nz_32 behaved rather differently, showing delayed aggregation, different mechanisms involved in the onset and growth of aggregation, and more organization by the end of the simulation period marked by larger differences in the column moist static energy between the moist and dry regions.

In nz_32, aggregation does not occur in the early period of the simulation because diabatically driven increases in the spatial variance of vertically integrated frozen moist static energy ($\langle h_f \rangle'^2$) by radiative processes and surface fluxes are too weak to overcome homogenization by horizontal circulations. More specifically, we suspect that nz_32's relatively high anvil cloud fraction and relative humidity inhibits radiative cooling in drier columns during the early period. Eventually, and for reasons which are not completely clear, nz_32 begins to aggregate in the latter half of the simulation. Interestingly, the intensity of its aggregation (quantified as $\langle h_f \rangle'^2$) eventually exceeds that of nz_64 and nz_128 by nearly a factor of 2. We believe this is due to its relatively weaker cold pools, which enable extreme drying of the boundary layer in dry columns. Conversely, relatively stronger cold pools in nz_64 and nz_128 maintain more homogeneous boundary layer moisture even after aggregation.

We note that the large domain simulations were initialized with equilibrated profiles of temperature and humidity from the small domain simulations. Because of the impact of vertical resolution on steady state relative humidity and temperature, large domain simulations were thus initiated with different profiles. It is possible that some of the simulated differences in convective aggregation, particularly time-to-onset for the nz_64 and nz_128 simulations, were affected by these differences in the initial profile. We are pacified by the results of the small domain simulations, which show that vertical resolution impacts mean state quantities in the absence of convective aggregation, including those important for aggregation (namely, radiative cooling and surface fluxes).

We wonder if the convective aggregation behavior of a large domain simulation with 256 vertical levels would be very different from nz_64 and nz_128. Due to computational limitations, we were unable to run a large domain simulation with 256 vertical levels. In the small domain simulations, nz_64 and nz_128 behaved somewhat similarly: both simulated similar (in both shape and magnitude) mean profiles of relative humidity and fractional detrainment rate. Both simulations also simulated a 6 km peak in quantities associated with enhanced congestus outflow. The nz_256 simulation, however, did not contain this peak, and simulated mean profiles of relative humidity and fractional detrainment were, by comparison, much lower than that of nz_64 and nz_256. Additionally, nz_256 was unique amongst the small domain simulations in that it began exhibiting signs of convective aggregation (increased $\langle hf \rangle'^2$ and reduced and more variable precipitable water). For example, would aggregation have enhanced congestus outflow in nz_256 as it did in nz_64, nz_128 and in previous studies (Sokol & Hartmann, 2022)? Or would it have behaved like nz_32, whose mid-tropospheric fractional detrainment profile, while larger in magnitude, displayed a similar shape to nz_256? This remains to be seen.

It is necessary to understand the sensitivity of deep convection to model formulation in order to interpret and apply simulations of deep convection for physical understanding and decision-making. For example, our results suggest that the vertical resolution of embedded CRMs in multi-scale climate models (through a process referred to as "superparameterization" or "multi-scale modeling framework" in which CRMs replace the convective parameterization) may impact the simulated mean global cloud and relative humidity fields, which in turn impacts the global radiative budget. Hence, in those models the vertical resolution of embedded CRMs may be a tunable parameter. CRMs are also commonly used to inform convective parameterizations, and there is a growing movement to use the output of CRMs to create data-driven (machine learning-derived) convective parameterizations. The variability of simulated deep convection with vertical resolution shown here, including the simulated magnitudes of certain physical processes (e.g., cold pool and mean radiative intensity) emphasizes the need to constrain convective parameterizations with observations. Lastly, CRMs with limited domains are one tool actively used to try and understand tropical anvil clouds and their response to warming (e.g., Mackie & Byrne, n.d.). Here we show that at least in one CRM, anvil cloud fraction is sensitive to vertical resolution. It remains to be seen whether the anvil cloud response to warming is similarly sensitive.

In summary, vertical resolution is an often overlooked free parameter in simulations of convection, especially of convective aggregation. In this study, we explore the impact of vertical resolution on the simulated behavior of deep convection, with a focus on convective aggregation. We find that vertical resolution directly impacts simulated profiles of clouds, temperature, and humidity, and affects the onset time of and equilibrium intensity of aggregated convection. The sensitivity of these simulations to vertical resolution is similar to the sensitivity of CRMs to turbulent mixing (Ohno et al., 2019; Jeevanjee & Zhou, 2022), which leads us to suspect that in the model used in this study (SAM), turbulent mixing is sensitive to vertical resolution. Furthermore, if our suspicion is correct (i.e., that differences in mixing are driving simulated differences in relative humidity and anvil cloud fraction), these results emphasize the need to improve the representation of simulated mixing processes in the atmosphere. Clearly, the consequences for simulating deep convection can be profound.

5 Open Research

SAM model code is publicly available at `http://rossby.msrc.sunysb.edu/~marat/SAM/`. Code to create the figures from model output is publicly available at `https://github.com/ajenney/conv_agg_vres_public`.

Acknowledgments
We thank Peter Blossey for help with SAM, and Zeyuan Hu and Adam Sokol for helpful discussions. This research has been supported by the National Oceanic and Atmospheric Administration Climate Global Change Postdoctoral Fellowship Program through UCAR CPAESS Grant no. NA18NWS4620043B. This research used computing resources of the Extreme Science and Engineering Discovery Environment (XSEDE) which was supported by National Science Foundation grant number ACI-1548562 (Towns et al., 2014) and allocation number TG-ATM190002.

References

Arnold, N. P., & Putman, W. M. (2018, April). Nonrotating convective Self-Aggregation in a limited area AGCM. *J Adv Model Earth Syst*, *10*(4), 1029–1046.

Becker, T., Stevens, B., & Hohenegger, C. (2017, June). Imprint of the convective parameterization and sea-surface temperature on large-scale convective self-aggregation. *J. Adv. Model. Earth Syst.*, *9*(2), 1488–1505.

Beydoun, H., Caldwell, P. M., Hannah, W. M., & Donahue, A. S. (2021, August). Dissecting anvil cloud response to sea surface warming. *Geophys. Res. Lett.*, *48*(15).

Beydoun, H., & Hoose, C. (2019, April). Aerosol-cloud-precipitation interactions in the context of convective self-aggregation. *J. Adv. Model. Earth Syst.*, *11*(4), 1066–1087.

Bretherton, C. S., Blossey, P. N., & Khairoutdinov, M. (2005, December). An Energy-Balance analysis of deep convective Self-Aggregation above uniform SST. *J. Atmos. Sci.*, *62*(12), 4273–4292.

Bretherton, C. S., Macvean, M. K., Bechtold, P., Chlond, A., Cotton, W. R., Cuxart, J., … Wyant, M. C. (1999, January). An intercomparison of radiatively driven entrainment and turbulence in a smoke cloud, as simulated by different numerical models. *Q.J Royal Met. Soc.*, *125*(554), 391–423.

Bryan, G. H., & Morrison, H. (2012, January). Sensitivity of a simulated squall line to horizontal resolution and parameterization of microphysics. *Mon. Weather Rev.*, *140*(1), 202–225.

Carpenter, R. L., Droegemeier, K. K., & Blyth, A. M. (1998, December). Entrainment and detrainment in numerically simulated cumulus congestus clouds. part i: General results. *J. Atmos. Sci.*, *55*(23), 3417–3432.

Carstens, J. D., & Wing, A. A. (2022, May). A spectrum of convective self-aggregation based on background rotation. *J. Adv. Model. Earth Syst.*, *14*(5).

Chen, Y.-T., & Wu, C.-M. (2019, October). The role of interactive SST in the cloud-resolving simulations of aggregated convection. *J. Adv. Model. Earth Syst.*, *11*(10), 3321–3340.

Clough, S. A., Shephard, M. W., Mlawer, E. J., Delamere, J. S., Iacono, M. J., Cady-Pereira, K., … Brown, P. D. (2005, March). Atmospheric radiative transfer modeling: a summary of the AER codes. *J. Quant. Spectrosc. Radiat. Transf.*, *91*(2), 233–244.

Coppin, D., & Bony, S. (2015, December). Physical mechanisms controlling the initiation of convective self-aggregation in a general circulation model. *J. Adv. Model. Earth Syst.*, *7*(4), 2060–2078.

Derbyshire, S. H., Beau, I., Bechtold, P., Grandpeix, J.-Y., Piriou, J.-M., Redelsperger, J.-L., & Soares, P. M. M. (2004, October). Sensitivity of moist convection to environmental humidity. *Quart. J. Roy. Meteor. Soc.*, *130*(604), 3055–3079.

Grant, L. D., & van den Heever, S. C. (2016, February). Cold pool dissipation. *J. Geophys. Res. D: Atmos.*, *121*(3), 1138–1155.

Gu, Y., Liou, K. N., Ou, S. C., & Fovell, R. (2011, March). Cirrus cloud simulations using WRF with improved radiation parameterization and increased vertical resolution. *J. Geophys. Res.*, *116*(D6).

Guo, Liu, Daum, Zeng, Li, & others. (2008). Effects of model resolution on entrainment (inversion heights), cloud-radiation interactions, and cloud radiative forcing. *Chem. Phys. Lipids*.

Held, I. M., Hemler, R. S., & Ramaswamy, V. (1993, December). Radiative-Convective equilibrium with explicit Two-Dimensional moist convection. *J. Atmos. Sci.*, *50*(23), 3909–3927.

Holloway, C. E., & Neelin, J. D. (2009, June). Moisture vertical structure, column water vapor, and tropical deep convection. *J. Atmos. Sci.*, *66*(6), 1665–1683.

Holloway, C. E., & Woolnough, S. J. (2016, January). The sensitivity of convective aggregation to diabatic processes in idealized radiative-convective equilibrium simulations. *Journal of Advances in Modeling Earth Systems*.

Huang, J.-d., & Wu, C.-M. (2022, March). A framework to evaluate convective aggregation: Examples with different microphysics schemes. *J. Geophys. Res.*, *127*(5).

Inness, P. M., Slingo, J. M., Woolnough, S. J., Neale, R. B., & Pope, V. D. (2001, July). Organization of tropical convection in a GCM with varying vertical resolution; implications for the simulation of the Madden-Julian oscillation. *Clim. Dyn.*, *17*(10), 777–793.

Jeevanjee, N., & Romps, D. M. (2013, March). Convective self-aggregation, cold pools, and domain size. *Geophys. Res. Lett.*, *40*(5), 994–998.

Jeevanjee, N., & Zhou, L. (2022, March). On the resolution-dependence of anvil cloud fraction and precipitation efficiency in radiative-convective equilibrium. *J. Adv. Model. Earth Syst.*, *14*(3).

Johnson, R. H., Ciesielski, P. E., & Hart, K. A. (1996). Tropical inversions near the 0 C level. *J. Atmos. Sci.*, *53*(13), 1838–1855.

Khairoutdinov, M. F., Krueger, S. K., Moeng, C.-H., Bogenschutz, P. A., & Randall, D. A. (2009, December). Large-eddy simulation of maritime deep tropical convection. *J. Adv. Model. Earth Syst.*, *2*(15).

Khairoutdinov, M. F., & Randall, D. A. (2003, February). Cloud resolving modeling of the ARM summer 1997 IOP: Model formulation, results, uncertainties, and sensitivities. *J. Atmos. Sci.*, *60*(4), 607–625.

Kuang, Z., & Bretherton, C. S. (2006). A Mass-Flux scheme view of a High-Resolution simulation of a transition from shallow to deep cumulus convection. *J. Atmos. Sci.*, *63*(7), 1895–1909.

Lee, E., Lee, E.-H., & Choi, I.-J. (2019, November). Impact of increased vertical resolution on Medium-Range forecasts in a global atmospheric model. *Mon. Weather Rev.*, *147*(11), 4091–4106.

Mackie, A., & Byrne, M. (n.d.). Effects of circulation on tropical cloud feedbacks in high-resolution simulations. *preprint manuscript submitted to Journal of Advances in Modeling Earth Systems*.

Mapes, B. E., & Houze, R. A. (1995, May). Diabatic divergence profiles in western pacific mesoscale convective systems. *Journal of the Atmospheric Sciences*, *52*(10), 1807–1828.

Mapes, B. E., & Zuidema, P. (1996, February). Radiative-Dynamical consequences of dry tongues in the tropical troposphere. *J. Atmos. Sci.*, *53*(4), 620–638.

Marchand, R., & Ackerman, T. (2010, August). An analysis of cloud cover in multiscale modeling framework global climate model simulations using 4 and 1 km horizontal grids. *J. Geophys. Res.*, *115*(D16).

Matsugishi, S., & Satoh, M. (2022, April). Sensitivity of the horizontal scale of convective self-aggregation to sea surface temperature in radiative convective equilibrium experiments using a global nonhydrostatic model. *J. Adv. Model. Earth Syst.*.

Mlawer, E. J., Taubman, S. J., Brown, P. D., Iacono, M. J., & Clough, S. A. (1997, July). Radiative transfer for inhomogeneous atmospheres: RRTM, a validated correlated-k model for the longwave. *J. Geophys. Res.*, *102*(D14), 16663–16682.

Molinari, J., Romps, D. M., Vollaro, D., & Nguyen, L. (2012, August). CAPE in tropical cyclones. *J. Atmos. Sci.*, *69*(8), 2452–2463.

Muller, C., & Bony, S. (2015, July). What favors convective aggregation and why? *Geophys. Res. Lett.*, *42*(13), 5626–5634.

Muller, C., & Held, I. M. (2012, August). Detailed investigation of the Self-Aggregation of convection in Cloud-Resolving simulations. *J. Atmos. Sci.*, *69*(8), 2551–2565.

Nuijens, L., & Emanuel, K. (2018). Congestus modes in circulating equilibria of the tropical atmosphere in a two-column model. *Quarterly Journal of the Royal*.

Ohno, T., & Satoh, M. (2018, August). Roles of cloud microphysics on cloud responses to sea surface temperatures in radiative-convective equilibrium experiments using a high-resolution global nonhydrostatic model. *J. Adv. Model. Earth Syst.*, *10*(8), 1970–1989.

Ohno, T., Satoh, M., & Noda, A. (2019, June). Fine vertical resolution radiative-convective equilibrium experiments: Roles of turbulent mixing on the high-cloud response to sea surface temperatures. *J. Adv. Model. Earth Syst.*, *11*(6), 1637–1654.

Parishani, H., Pritchard, M. S., Bretherton, C. S., Wyant, M. C., & Khairoutdinov, M. (2017, July). Toward low-cloud-permitting cloud superparameterization with explicit boundary layer turbulence: LOW-CLOUD ULTRAPARAMETERIZATION. *J. Adv. Model. Earth Syst.*, *9*(3), 1542–1571.

Patrizio, C. R., & Randall, D. A. (2019, July). Sensitivity of convective self-aggregation to domain size. *J. Adv. Model. Earth Syst.*, *11*(7), 1995–2019.

Pauluis, O., & Garner, S. (2006, July). Sensitivity of Radiative–Convective equilibrium simulations to horizontal resolution. *J. Atmos. Sci.*, *63*(7), 1910–1923.

Posselt, D. J., van den Heever, S. C., & Stephens, G. L. (2008, April). Trimodal cloudiness and tropical stable layers in simulations of radiative convective equilibrium. *Geophys. Res. Lett.*, *35*(8).

Retsch, M. H., Hohenegger, C., & Stevens, B. (2017, October). Vertical resolution refinement in an aqua-planet and its effect on the ITCZ. *J. Adv. Model. Earth Syst.*, *9*(6), 2425–2436.

Roeckner, E., Brokopf, R., Esch, M., Giorgetta, M., Hagemann, S., Kornblueh, L., ... Schulzweida, U. (2006, August). Sensitivity of simulated climate to horizontal and vertical resolution in the ECHAM5 atmosphere model. *J. Clim.*, *19*(16), 3771–3791.

Romps, D. M. (2014, October). An analytical model for tropical relative humidity. *J. Clim.*, *27*(19), 7432–7449.

Romps, D. M., & Kuang, Z. (2010, February). Do undiluted convective plumes exist in the upper tropical troposphere? *J. Atmos. Sci.*, *67*(2), 468–484.

Schulz, H., & Stevens, B. (2018, October). Observing the tropical atmosphere in moisture space. *J. Atmos. Sci.*, *75*(10), 3313–3330.

Seeley, J. T., Jeevanjee, N., Langhans, W., & Romps, D. M. (2019, January). Formation of tropical anvil clouds by slow evaporation. *Geophys. Res. Lett.*, *46*(1), 492–501.

Seiki, T., Kodama, C., Satoh, M., Hashino, T., Hagihara, Y., & Okamoto, H. (2015, May). Vertical grid spacing necessary for simulating tropical cirrus clouds with a high-resolution atmospheric general circulation model. *Geophysical Research Letters*, *42*(10), 4150–4157.

Singh, M. S., & O'Gorman, P. A. (2013). Influence of entrainment on the thermal stratification in simulations of radiative-convective equilibrium. *Geophys. Res. Lett.*, *40*(16), 4398–4403.

Singh, M. S., & O'Gorman, P. A. (2015, October). Increases in moist-convective updraught velocities with warming in radiative-convective equilibrium: Increases in updraught velocities with warming. *Q.J.R. Meteorol. Soc.*, *141*(692), 2828–2838.

Singh, M. S., Warren, R. A., & Jakob, C. (2019, December). A steady-state model for the relationship between humidity, instability, and precipitation in the tropics. *J. Adv. Model. Earth Syst.*, *11*(12), 3973–3994.

Sokol, A. B., & Hartmann, D. L. (2022, June). Congestus mode invigoration by convective aggregation in simulations of radiative-convective equilibrium. *J. Adv. Model. Earth Syst.*.

Stevens, B., Lenschow, D. H., Faloona, I., Moeng, C.-H., Lilly, D. K., Blomquist, B.,

... Thornton, D. (2003, October). On entrainment rates in nocturnal marine stratocumulus. *Quart. J. Roy. Meteor. Soc.*, *129*(595), 3469–3493.

Stevens, B., Moeng, C.-H., Ackerman, A. S., Bretherton, C. S., Chlond, A., de Roode, S., ... Zhu, P. (2005, June). Evaluation of Large-Eddy simulations via observations of nocturnal marine stratocumulus. *Mon. Weather Rev.*, *133*(6), 1443–1462.

Tobin, I., Bony, S., & Roca, R. (2012, October). Observational evidence for relationships between the degree of aggregation of deep convection, water vapor, surface fluxes, and radiation. *J. Clim.*, *25*(20), 6885–6904.

Tompkins, A. M., & Emanuel, K. A. (2000). The vertical resolution sensitivity of simulated equilibrium temperature and water-vapour profiles. *Quart. J. Roy. Meteor. Soc.*, *126*(565), 1219–1238.

Tompkins, A. M., & Semie, A. G. (2017, June). Organization of tropical convection in low vertical wind shears: Role of updraft entrainment. *J. Adv. Model. Earth Syst.*, *9*(2), 1046–1068.

Wang, X., Zhang, G. J., & Wang, Y. (2022, January). Evaluating and improving scale-awareness of a convective parameterization closure using cloud-resolving model simulations of convection. *J. Geophys. Res.*, *127*(2).

Wing, A. A., & Cronin, T. W. (2016). Self-aggregation of convection in long channel geometry. *Quarterly Journal of the Royal*.

Wing, A. A., Emanuel, K., Holloway, C. E., & Muller, C. (2017, November). Convective Self-Aggregation in numerical simulations: A review. *Surv. Geophys.*, *38*(6), 1173–1197.

Wing, A. A., & Emanuel, K. A. (2014, March). Physical mechanisms controlling self-aggregation of convection in idealized numerical modeling simulations: SELF-AGGREGATION MECHANISMS. *J. Adv. Model. Earth Syst.*, *6*(1), 59–74.

Wing, A. A., Reed, K. A., Satoh, M., Stevens, B., Bony, S., & Ohno, T. (2018, March). Radiative–convective equilibrium model intercomparison project. *Geoscientific Model Development*, *11*(2), 793–813.

Wing, A. A., Stauffer, C. L., Becker, T., Reed, K. A., Ahn, M., Arnold, N. P., ... Zhao, M. (2020, July). Clouds and convective Self-Aggregation in a Multi-Model ensemble of Radiative-Convective equilibrium simulations. *J. Adv. Model. Earth Syst.*.

Yanase, T., Nishizawa, S., Miura, H., Takemi, T., & Tomita, H. (2020, August). New critical length for the onset of self-aggregation of moist convection. *Geophys. Res. Lett.*, *47*(16).

Zipser, E. J. (2003). Some views on "hot towers" after 50 years of tropical field programs and two years of TRMM data. In W.-K. Tao & R. Adler (Eds.), *Cloud systems, hurricanes, and the tropical rainfall measuring mission (TRMM): A tribute to dr. joanne simpson* (pp. 49–58). Boston, MA: American Meteorological Society.